Velocity-space observation regions of high-resolution two-step reaction gamma-ray spectroscopy

Salewski, Mirko; Nocente, M.; Gorini, G.; Jacobsen, Asger Schou; Kiptily, V.G.; Korsholm, Søren Bang; Leipold, Frank; Madsen, Jens; Moseev, D.; Nielsen, Stefan Kragh

Total number of authors:
13

Published in:
Nuclear Fusion

Link to article, DOI:
10.1088/0029-5515/55/9/093029

Publication date:
2015

Document Version
Peer reviewed version

25 September 2015

Velocity-space observation regions of high-resolution two-step reaction gamma-ray spectroscopy

M. Salewski[1], M. Nocente[2,3], G. Gorini[2,3], A.S. Jacobsen[1], V.G. Kiptily[4], S.B. Korsholm[1], F. Leipold[1], J. Madsen[1], D. Moseev[5], S.K. Nielsen[1], J. Rasmussen[1], M. Stejner[1], M Tardocchi[3] and JET Contributors[6]‡

[1] Technical University of Denmark, Department of Physics, DK-2800 Kgs. Lyngby, Denmark

[2] University of Milano Bicocca, Department of Physics, Milano 20126, Italy

[3] Istituto di Fisica del Plasma, Consiglio Nazionale delle Ricerche, Milano 20125, Italy

[4] CCFE, Culham Science Centre, Abingdon, Oxon, X14 3DB, UK

[5] Max Planck Institute for Plasma Physics, 17491 Greifswald, Germany

[6] EUROfusion Consortium, JET, Culham Science Centre, Abingdon, OX14 3DB, UK

E-mail: `msal@fysik.dtu.dk`

Abstract. High-resolution γ-ray spectroscopy (GRS) measurements resolve spectral shapes of Doppler-broadened γ-rays. We calculate weight functions describing velocity-space sensitivities of any two-step reaction GRS measurements in magnetized plasmas using the resonant nuclear reaction $^9\mathrm{Be}(\alpha, \mathrm{n}\gamma)^{12}\mathrm{C}$ as an example. The energy-dependent cross sections of this reaction suggest that GRS is sensitive to alpha particles above about 1.7 MeV and highly sensitive to alpha particles at the resonance energies of the reaction. Here we demonstrate that high-resolution two-step reaction GRS measurements are not only selective in energy but also in pitch angle. They can be highly sensitive in particular pitch angle ranges and completely insensitive in others. Moreover, GRS weight functions allow rapid calculation of γ-ray energy spectra from fast-ion distribution functions, additionally revealing how many photons any given alpha-particle velocity-space region contributes to the measurements in each γ-ray energy bin.

1. Introduction

Gamma-ray spectroscopy (GRS) is an essential diagnostic to study fast ions in fusion plasmas [1, 2]. Early GRS measurements in tokamaks have been made at Doublet-III [3], TFTR [4], JET [5–13] and JT-60U [14, 15]. More recently, high-resolution GRS measurements have been made at JET [16–21] and ASDEX Upgrade [22] thanks to the development of new detectors [18, 23]. GRS is particularly well-suited for large, hot

‡ See the Appendix of F. Romanelli et al., Proceedings of the 25th IAEA Fusion Energy Conference 2014, Saint Petersburg, Russia

devices such as JET [5–13, 16–21], ITER [24] or DEMO [25] since high temperatures enhance fusion reaction rates and hence γ-ray fluxes [1, 2].

Many nuclear reactions in hot fusion plasmas lead to γ-ray emission [1, 2]. At JET, several species including alpha particles, helium-3, deuterium or hydrogen have been measured using GRS [5–13, 16–21]. These fast ions are generated in fusion reactions, by ion cyclotron resonance heating (ICRH) or by neutral beam injection (NBI) [7]. γ-rays are emitted when fast ions react with bulk plasma ions or with low-mass impurities such as lithium, beryllium, boron, carbon or oxygen [7]. Fast alpha particles are of particular interest as they are produced at an energy of 3.5 MeV in the most important fusion reaction T(D,n)α, which will release most of the fusion power in future burning plasmas. Fast alpha particles can undergo resonant nuclear reactions with low-mass impurities allowing GRS measurements with high signal-to-noise ratio [26]. Here we consider the reaction $^9\mathrm{Be}(\alpha, \mathrm{n}\gamma)^{12}\mathrm{C}$ [8, 27], which has been proposed for studies of alpha particles in ITER where beryllium is the first-wall material. This reaction has regularly been studied at JET [7–10, 12, 16, 17, 19, 21] and has become all the more important at JET since the installation of the ITER-like beryllium wall [28, 29]. The reaction happens in two steps. 1) An alpha particle and ^{9}Be react to form excited $^{12}\mathrm{C}^*$ and a neutron. 2) The excited $^{12}\mathrm{C}^*$ rapidly decays to ground-state ^{12}C emitting a γ-photon:

$$\alpha + {}^9\mathrm{Be} \rightarrow {}^{12}\mathrm{C}^* + \mathrm{n}, \tag{1}$$

$$^{12}\mathrm{C}^* \rightarrow {}^{12}\mathrm{C} + \gamma. \tag{2}$$

The energy release of the reaction is $Q = 5.70$ MeV of which $E_{\gamma 0} = 4.44$ MeV is required to populate the excited state $^{12}\mathrm{C}^*$. This is also the rest frame energy of the γ-photon that is emitted when $^{12}\mathrm{C}^*$ decays to the ground state. The remaining $Q^* = 1.26$ MeV becomes kinetic energy of the reaction products $^{12}\mathrm{C}^*$ and the neutron in addition to the initial kinetic energies of the fast alpha and the thermal ^{9}Be. γ-photons are Doppler-shifted due to the velocity component u_C of the $^{12}\mathrm{C}^*$ nucleus along the line-of-sight of the detector. The Doppler-shifted energy E_γ of the detected γ-photon is

$$E_\gamma = E_{\gamma 0}\left(1 + \frac{u_C}{c}\right) \tag{3}$$

where c is the speed of light and u_C/c is typically on the order of 1%.

Each nuclear reaction emitting γ-rays forms a peak in the measured energy spectra. Such peaks are hence broadened by the Doppler shift according to equation 3. Recently, it has become possible to measure the spectral shapes of such peaks using high-resolution γ-ray spectrometers [2, 16–21]. Here we study sensitivities of such high-resolution GRS measurements to 2D fast-ion distribution functions typical for hot, magnetized plasmas. It is known from the energy dependence of the reaction cross sections (figure 1) that GRS measurements are highly sensitive to alpha particles near the resonance energies of the reaction at 1.9 MeV, 2.6 MeV, 4.0 MeV, 4.5 MeV, 5.0 MeV, 5.3 MeV and 5.75 MeV [30]. As the energies of thermal ^{9}Be impurities are negligible compared with the alpha particle energies, resonance peaks appear as semi-circular ridges in figure 1. The sensitivity to alpha particles with energies below 1.7 MeV is poor. (At 1.7 MeV the

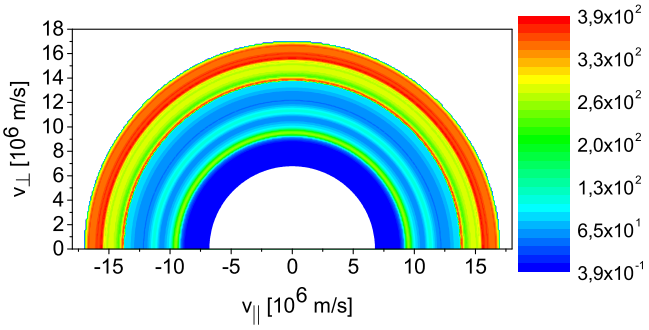

Figure 1. Reaction cross sections [millibarn] of the ^{9}Be(α,nγ)^{12}C reaction as a function of $(v_\parallel, v_\perp)$ of the alpha particle for energies up to 6 MeV corresponding to a velocity magnitude $v = 17 \times 10^6$ m/s. The resonances appear at $v = (9.5, 11.1, 13.8, 14.7, 15.5, 15.9, 16.6) \times 10^6$ m/s. Below the resonance at 1.9 MeV ($v = 9 \times 10^6$ m/s) the cross sections become very small, and hence GRS is insensitive to particles populating the inner white region.

sensitivity is about 10% of the sensitivity at the resonance maximum at 1.9 MeV). In this paper we show that the energies of the measured γ-photons from a particular reaction indicate not only the energies of the alpha particles but also their pitches. The pitch is defined as $p = v_\parallel/v$ where $v_\parallel$ is the velocity component parallel to the magnetic field and v is the velocity magnitude. Energy and momentum conservation imply, together with the reaction cross sections, the existence of regions in 2D velocity space to which a measurement in a given energy range of the γ-photon is sensitive as well as regions to which the measurement is completely insensitive.

Such 2D velocity-space sensitivities of two-step reaction GRS measurements are described by weight functions analogous to those of fast-ion D_α (FIDA) [31, 32], collective Thomson scattering (CTS) [32,33] and neutron emission spectrometry (NES) measurements [34, 35]. Our final goal is to infer 2D fast-ion velocity distribution functions by tomographic inversion using weight functions as we present here for GRS [33, 36, 37]. Whereas full tomographic inversion of GRS measurements cannot yet be achieved, the general method has been demonstrated using FIDA measurements at ASDEX Upgrade in MHD quiescent plasmas [37,38] and in plasmas with sawteeth [39]. A comparison of the tomographic inversion before and after a sawtooth crash showed a strong dependence of the fast-ion redistribution on pitch. Whereas these measurements relied on FIDA, all available fast-ion diagnostics can in principle be combined, provided their weight functions are known [40]. Here we focus on three other useful applications of weight functions. First, weight functions provide significant insight into the velocity-space sensitivity of the diagnostic. They separate observable velocity-space regions from unobservable regions [31–35, 41–62]. Second, they reveal the velocity-space origin of a measurement for a given 2D fast-ion velocity distribution function [31–35, 41, 56–61, 63]. Third, they allow rapid calculation of synthetic measurements [32–35]. The formalism

we present here allows these applications for two-step reaction GRS measurements.

In section 2 we show how to calculate GRS weight functions numerically using the GENESIS code as forward model [20,64]. We present numerically calculated GRS weight functions to show the velocity-space observation regions typical for high-resolution GRS measurments at JET in section 3. To gain insight into the numerically calculated GRS weight functions, we consider the kinematics of the $^9\mathrm{Be}(\alpha, \mathrm{n}\gamma)^{12}\mathrm{C}$ reaction based on energy and momentum conservation in section 4, which allows us to construct a tractable simplified model showing observable regions in section 5. We compare analytical and numerical approaches in section 6. In section 7 we study the dependence of the GRS velocity-space sensitivities on key parameters. We calculate GRS measurements using weight functions in section 8 and show where in velocity space the measurements originate from for typical JET parameters. We discuss the potential application of GRS weight functions in future burning plasmas in section 9 and conclude in section 10.

2. Numeric computation of GRS weight functions

Weight functions, w, relate 2D fast-ion distribution functions, f, to measurements, s, according to [31–35, 41]

$$s(E_{\gamma,1}, E_{\gamma,2}, \phi) = \int_{vol} \int_0^\infty \int_{-\infty}^\infty w(E_{\gamma,1}, E_{\gamma,2}, \phi, v_\parallel, v_\perp, \mathbf{x}) f(v_\parallel, v_\perp, \mathbf{x}) dv_\parallel dv_\perp d\mathbf{x}. \quad (4)$$

For GRS measurements, $s(E_{\gamma,1}, E_{\gamma,2}, \phi)$ is the detection rate of γ-rays [photons/s] in the energy range $E_{\gamma,1} < E_\gamma < E_{\gamma,2}$ with a viewing angle ϕ between the line-of-sight of the GRS diagnostic and the magnetic field. $(v_\parallel, v_\perp)$ are the velocities parallel and perpendicular to the magnetic field, respectively, and $\mathbf{x}$ describes the spatial coordinates. We use 2D $(v_\parallel, v_\perp)$-coordinates rather than the equivalent and more widespread (energy, pitch)-coordinates for example used in the TRANSP code as our expressions are simpler in $(v_\parallel, v_\perp)$-coordinates. The fast-ion velocity distribution function f is a 2D function due to rotational symmetry of the full 3D fast-ion velocity distribution function. It is obtained by transforming to cylindrical coordinates and integrating over the ignorable gyroangle Γ: $f^{2D} = 2\pi v_\perp f^{3D}$. In cylindrical coordinates $v_\parallel$ can be negative or positive whereas $v_\perp$ is always positive. The units of f in equation 4 are $[\mathrm{s}^2/\mathrm{m}^5]$ due to multiplication of f^{3D} with the Jacobian $v_\perp$. The units of GRS weight functions are thus [photons / (α-particle $\times$ s)].

Weight functions of any fast-ion diagnostic can be found numerically using a forward model that can predict a measurement for an arbitrary fast-ion distribution function. In this numerical approach we calculate energy spectra of γ-rays emitted due to a small collection of N_f fast alpha particles whose velocities $(v_\parallel, v_\perp)$ are varied to scan the area of interest in velocity space. This formalism is analogous to numeric computation of weight functions for FIDA [31, 38], CTS [33] and NES [34, 35]. This collection of fast ions at phase-space position $(\mathbf{x}_0, v_{\parallel 0}, v_{\perp 0})$ has a fast-ion distribution function f_δ of the form

$$f_\delta(v_\parallel, v_\perp, \mathbf{x}) = N_f \delta(v_\parallel - v_{\parallel 0}) \delta(v_\perp - v_{\perp 0}) \delta(\mathbf{x} - \mathbf{x}_0). \quad (5)$$

Substitution into equation 4 and integration gives the amplitude of the weight function at phase-space position $(\mathbf{x}_0, v_{\parallel 0}, v_{\perp 0})$:

$$w(E_{\gamma,1}, E_{\gamma,2}, \phi, v_{\parallel 0}, v_{\perp 0}, \mathbf{x}_0) = \frac{s_\delta(E_{\gamma,1}, E_{\gamma,2}, \phi)}{N_f}. \tag{6}$$

GRS weight functions show the incident rate of γ-photons between two γ-ray energies viewed at angle ϕ per alpha particle at phase-space position $(\mathbf{x}_0, v_{\parallel 0}, v_{\perp 0})$.

3. Observable regions of GRS measurements at JET

In this section we calculate GRS weight functions by the numerical approach given in equation 6 using the GENESIS code. Figures 2 and 3 show weight functions for observation angles of respectively $\phi = 90°$ and $\phi = 30°$ at Doppler shifts typical for high-resolution GRS measurements at JET. The coloured regions are observable whereas the white regions are unobservable. The amplitude shows the sensitivity of the measurement in [photons/(α-particle $\times$ s)]. GRS measurements are indeed insensitive to energies below about 1.7 MeV and are most sensitive to alpha particles with energies at the resonance energies. These features are inherited from the cross sections of the reaction shown in figure 1. However, the weight functions reveal that GRS measurements are also highly selective in pitch.

For an observation angle of $\phi = 90°$ and large Doppler shifts ($\Delta E_\gamma = E_\gamma - E_{\gamma 0} \gtrsim 45$ keV), GRS measurements are completely insensitive to ions with pitches $\sim \pm 1$. The unobservable regions become larger for larger Doppler shifts such that for very large Doppler shifts ($\Delta E_\gamma \sim 90$ keV), the measurements are only sensitive to pitches around zero. We will show in the following sections that the energy and momentum equations cannot be obeyed in the unobservable regions between 1.7 MeV and 6 MeV. Hence γ-photons with the given Doppler shifts cannot originate from these regions. For a Doppler shift of $\Delta E_\gamma \sim 30$ keV, the sensitivity of GRS measurements depends only weakly on the pitch. For low Doppler shifts ($\Delta E_\gamma \lesssim 15$ keV), the measurements are most sensitive to particles with pitches close to ± 1 on all resonances. We will explain this perhaps surprising result as a consequence of energy and momentum conservation as well as the projection of $\mathbf{v}_c$ onto the line-of-sight in section 7. The redshifted side is identical to the blueshifted side at the same Doppler shift magnitude (figure 2 (a) and (c)) corresponding to the expectation to observe spectra that are symmetric about the peak energy.

We illustrate typical velocity-space observation regions of the other high-resolution γ-ray spectrometer at an observation angle $\phi = 30°$ and various Doppler shifts in figure 3. For any Doppler shift there are pitch ranges that are completely unobservable at $\phi = 30°$. As for $\phi = 90°$ the unobservable regions grow with the Doppler shift. The observable regions are now biased towards either positive or negative pitches. The blueshifted side ($\Delta E_\gamma > 0$) is most sensitive to co-going particles for large Doppler shifts ($\Delta E_\gamma \gtrsim 30$ keV). For very large Doppler shifts ($\Delta E_\gamma \gtrsim 75$ keV) the measurement is not sensitive to particles with negative pitches at all. The redshifted side is always a

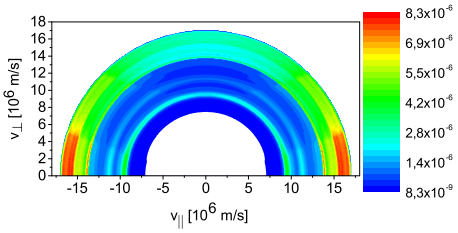

(a) $\Delta E_\gamma = -15$ keV

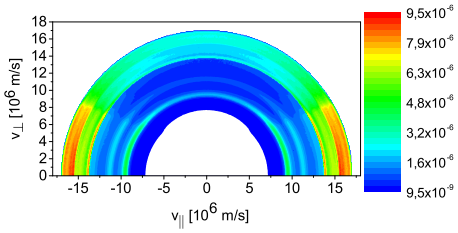

(b) $\Delta E_\gamma = 0$ keV

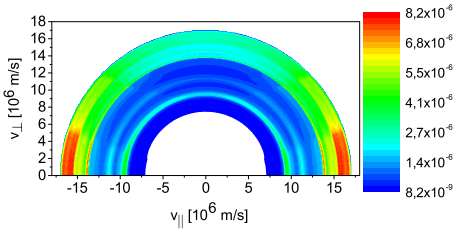

(c) $\Delta E_\gamma = 15$ keV

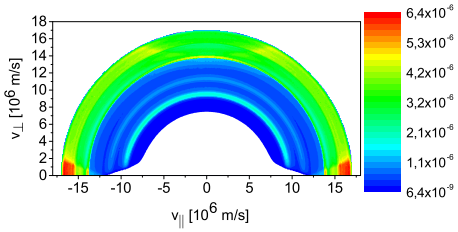

(d) $\Delta E_\gamma = 30$ keV

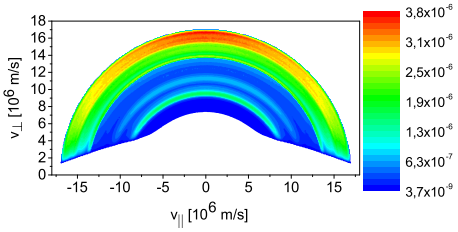

(e) $\Delta E_\gamma = 45$ keV

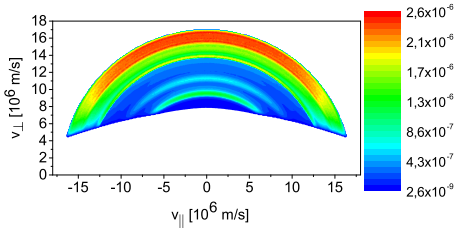

(f) $\Delta E_\gamma = 60$ keV

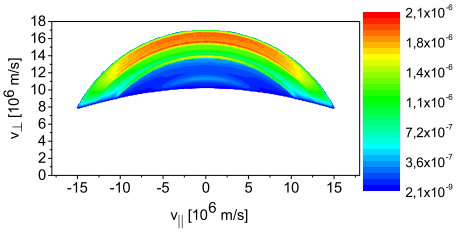

(g) $\Delta E_\gamma = 75$ keV

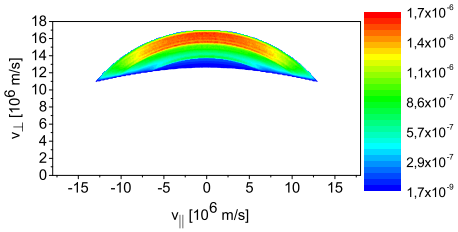

(h) $\Delta E_\gamma = 90$ keV

Figure 2. Full GRS weight functions w [photons / (α-particle $\times$ s)] for $\phi = 90°$ and various Doppler-shifted energies ΔE_γ of the γ-photons. The γ-ray energy bin width is $E_{\gamma,1} - E_{\gamma,2} = 1$ keV. We assume $n_{Be} = 10^{18}$ m^{-3}. Note that the colour scale is different in each plot.

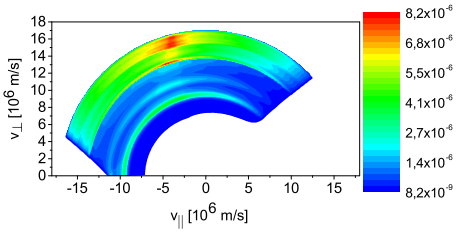

(a) $\Delta E_\gamma = -15$ keV

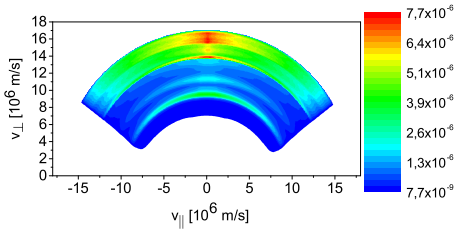

(b) $\Delta E_\gamma = 0$ keV

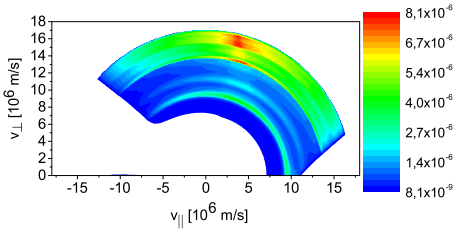

(c) $\Delta E_\gamma = 15$ keV

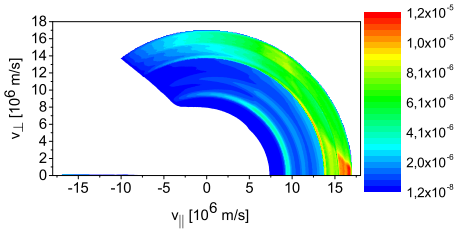

(d) $\Delta E_\gamma = 30$ keV

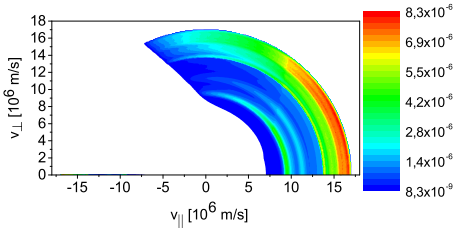

(e) $\Delta E_\gamma = 45$ keV

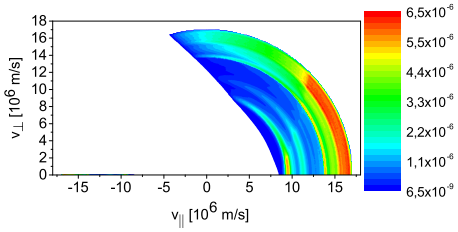

(f) $\Delta E_\gamma = 60$ keV

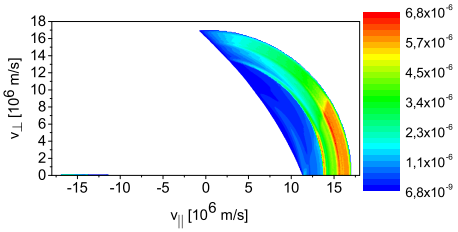

(g) $\Delta E_\gamma = 75$ keV

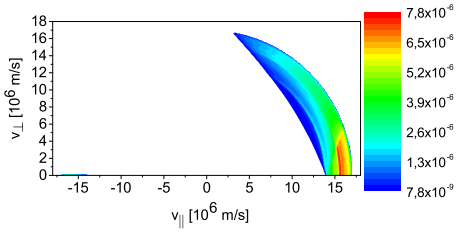

(h) $\Delta E_\gamma = 90$ keV

Figure 3. Full GRS weight functions w [photons / (α-particle $\times$ s)] for $\phi = 30°$ and various Doppler-shifted energies ΔE_γ of the γ-photons. The γ-ray energy bin width is $E_{\gamma,1} - E_{\gamma,2} = 1$ keV. We assume $n_{Be} = 10^{18}$ m^{-3}. Note that the colour scale is different in each plot.

mirror image of the blueshifted side at the same Doppler shift magnitude (figure 3 (a) and (c)). For low Doppler shifts ($\Delta E_\gamma \lesssim 15$ keV), the measurements are most sensitive to trapped particles with pitches close to zero. This again perhaps surprising result will also be explained in section 7.

Thus we find that firstly GRS measurements are highly selective in pitch depending on the observation angle and the Doppler shift. Secondly, the pitch selectivity for both view changes depending on the Doppler shift. The latter is perhaps a surprising result that we will study using an analytic approach in the following sections.

4. Kinematics of the ^{9}Be$(\alpha, \mathrm{n}\gamma)^{12}$C reaction

The numeric computations of GRS weight functions is the most accurate way to characterize the velocity-space sensitivity of GRS measurements as the numeric GRS weight functions account for all physics modelled in the GENESIS code including the anisotropic differential cross sections of the ^{9}Be$(\alpha, \mathrm{n}\gamma)^{12}$C reaction [65]. However, the numeric approach provides limited insight and, for example, does not explain why large pitch ranges are not observable. In the following sections we seek to gain insight into the velocity-space sensitivity of GRS measurements by constructing a simplified model of GRS weight functions based on the kinematics of the ^{9}Be$(\alpha, \mathrm{n}\gamma)^{12}$C reaction. The gyro-angle Γ of the alpha particle at the time of the reaction influences the measurable Doppler-shifted energy E_γ of a γ-photon emitted by ^{12}C* due to conservation of energy and momentum. Motion of the alpha towards the detector tends to lead to blueshift whereas motion of the alpha away from the detector tends to lead to redshift. Here we establish this functional dependence. E_γ depends linearly on the line-of-sight velocity u_C of the carbon nucleus according to equation 3. u_C in turn can be related to the gyro-angle Γ of the alpha particle by energy and momentum conservation.

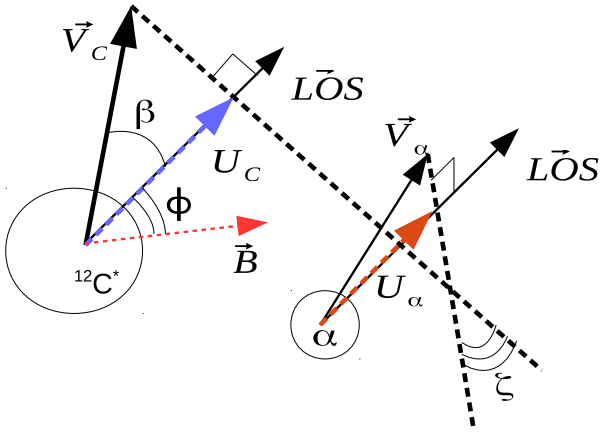

Figure 4. Sketch of the geometric relation between the magnetic field, the line-of-sight (LOS) and the velocities of the ^{12}C* nucleus, $\mathbf{v}_C$, and the alpha particle, $\mathbf{v}_\alpha$. The respective line-of-sight velocities are u_c and u_α. The dashed lines are perpendicular to the line-of-sight. The angles ϕ, β, ζ are defined as $\phi = \angle(\hat{\mathbf{v}}_{LOS}, \mathbf{B})$, $\beta = \angle(\hat{\mathbf{v}}_{LOS}, \mathbf{v}_C)$ and $\zeta = \angle(\hat{\mathbf{v}}_{\perp\alpha,LOS}, \hat{\mathbf{v}}_{\perp C,LOS})$.

Our formalism is analogous to that for neutron emission spectrometry (NES) [35]. However, two nuisance parameters appear as the reaction kinematics in two-step reaction GRS is less constrained than in NES which relies on one-step reactions. In one-step reaction NES we know the energy as well as the momentum of the neutrons produced in the reaction since only neutrons moving along the line-of-sight towards the detector are measured. In two-step reaction GRS measurements we neither know the energy nor the momentum of the $^{12}C^*$ produced in the reaction, but we know its velocity component u_C along the line-of-sight of the γ-ray detector as we know the energy of the γ-photon. The other two directions are described by the unknown angles β and ζ. These angles and the velocities and line-of-sight velocities of the $^{12}C^*$ and of the alpha particle relative to the line-of-sight and the local magnetic field are sketched in figure 4.

We neglect the gyro-motion of the $^{12}C^*$ as it decays after much shorter time than the cyclotron period. The decay time can be estimated from the intrinsic half-width of the 4.44 MeV level, $\Delta E_{\gamma 0} = 5.4$ meV, to $\hbar/\Delta E_{\gamma 0} \sim 61$ fs [66] where $\hbar$ is the reduced Planck constant. The cyclotron period of fully ionized $^{12}C^*$ is about 60 ns for a magnetic field of 2.2 T, i.e. $\sim 10^6$ times larger. In our simplified model, we further neglect the energy and momentum of the thermal ^{9}Be impurities compared with the energy and momentum of the alpha particle. For a beryllium temperature of ~ 10 keV and an alpha particle energy of 2 MeV, the alpha-to-beryllium energy ratio is ~ 200 and the momentum ratio is ~ 10. The GENESIS code accounts for the non-zero energy and momentum of beryllium. A calculation showed that non-zero beryllium temperatures blur the GRS weight functions somewhat but preserve their large-scale features. We do not show these temperature effects for brevity.

Hence the energy and momentum conservation equations for the first step (equation 1) of the two-step reaction become, respectively,

$$\frac{1}{2}m_\alpha v_\alpha^2 + Q^* = \frac{1}{2}m_C v_C^2 + \frac{1}{2}m_n v_n^2, \tag{7}$$

$$m_\alpha \mathbf{v}_\alpha = m_C \mathbf{v}_C + m_n \mathbf{v}_n \tag{8}$$

where subscripts α, C and n refer to the alpha particle, the ^{12}C and the neutron, respectively. We solve equation 8 for $\mathbf{v}_n$ and eliminate v_n^2 from the energy equation:

$$\frac{1}{2}m_\alpha v_\alpha^2 + Q^* = \frac{1}{2}m_C v_C^2 + \frac{1}{2m_n}(m_\alpha^2 v_\alpha^2 + m_C^2 v_C^2 - 2m_\alpha m_C \mathbf{v}_\alpha \cdot \mathbf{v}_C). \tag{9}$$

When equation 9 is solved for v_α, the solution may not conserve momentum but instead comply with $m_\alpha \mathbf{v}_\alpha = m_C \mathbf{v}_C - m_n \mathbf{v}_n$ rather than the correct momentum equation. This is checked for and excluded below. The dot product $\mathbf{v}_\alpha \cdot \mathbf{v}_C$ in equation 9 is calculated by introducing the line-of-sight velocities. The line-of-sight velocity u_C of ^{12}C can at once be calculated from the measured energies E_γ in high-resolution GRS according to equation 3. The line-of-sight velocity u_α of the alpha leaves a signature in the γ-ray spectra through the momentum and the energy equations whereas its velocity perpendicular to the line-of-sight enters through the energy equation only. Motivated by this observation, we split the velocity vectors of the ^{12}C and the alpha into components

parallel and perpendicular to the line-of-sight,

$$\mathbf{v}_\alpha = u_\alpha \hat{\mathbf{v}}_{LOS} + \sqrt{v_\alpha^2 - u_\alpha^2}\hat{\mathbf{v}}_{\perp\alpha,LOS}, \tag{10}$$

$$\mathbf{v}_C = u_C \hat{\mathbf{v}}_{LOS} + \sqrt{v_C^2 - u_C^2}\hat{\mathbf{v}}_{\perp C,LOS} \tag{11}$$

where $\hat{\mathbf{v}}_{LOS}$ is the unit vector along the line-of-sight towards the detector and $\hat{\mathbf{v}}_{\perp\alpha,LOS}$ and $\hat{\mathbf{v}}_{\perp C,LOS}$ are unit vectors of the velocity components of the alpha particle and the carbon nucleus perpendicular to the line-of-sight, respectively. The line-of-sight velocity u_C and the total velocity v_C can be related according to

$$u_C = v_C \cos\beta \tag{12}$$

where $\beta \in [0, \pi]$ is the angle between $\hat{\mathbf{v}}_C$ and $\hat{\mathbf{v}}_{LOS}$ as sketched in figure 4. β is a random variable with a probability distribution which we will sample by Monte Carlo simulations. As v_C is the magnitude of $\mathbf{v}_C$, u_C and $\cos\beta$ have the same sign.

The dot product in equation 9 becomes

$$\mathbf{v}_\alpha \cdot \mathbf{v}_C = u_\alpha u_C + \cos\zeta\sqrt{(v_\alpha^2 - u_\alpha^2)(v_C^2 - u_C^2)} \tag{13}$$

where $\zeta \in [0, 2\pi]$ is the angle between $\hat{\mathbf{v}}_{\perp\alpha,LOS}$ and $\hat{\mathbf{v}}_{\perp C,LOS}$ as sketched in figure 4. ζ is, as β, a random variable with a probability distribution which we sample by Monte Carlo simulation. For the special cases that $\mathbf{v}_\alpha$ or $\mathbf{v}_C$ has no velocity component perpendicular to the line-of-sight, the dot product becomes

$$\mathbf{v}_\alpha \cdot \mathbf{v}_C = u_\alpha u_C \tag{14}$$

as $u_\alpha^2 = v_\alpha^2$ or $u_C^2 = v_C^2$. Then ζ is not defined, and the simplified dot product must be used. This simplified dot product appears for NES weight functions because detectable neutrons always move along the line-of-sight [35]. Substituting equation 13 into equation 9 we get

$$\begin{aligned}&\frac{1}{2}(m_\alpha - \frac{m_\alpha^2}{m_n})v_\alpha^2 + Q^* = \frac{1}{2}(m_C + \frac{m_C^2}{m_n})v_C^2 \\ &- \frac{m_\alpha m_C}{m_n}\Big(u_\alpha u_C + \cos\zeta\sqrt{(v_\alpha^2 - u_\alpha^2)(v_C^2 - u_C^2)}\Big).\end{aligned} \tag{15}$$

We eliminate v_C for $\beta \neq \pi/2$:

$$\begin{aligned}&\frac{1}{2}(m_\alpha - \frac{m_\alpha^2}{m_n})v_\alpha^2 + Q^* = \frac{1}{2}(m_C + \frac{m_C^2}{m_n})\frac{u_C^2}{\cos^2\beta} \\ &- \frac{m_\alpha m_C}{m_n}\Big(u_\alpha u_C + \cos\zeta\sqrt{(v_\alpha^2 - u_\alpha^2)(u_C^2/\cos^2\beta - u_C^2)}\Big).\end{aligned} \tag{16}$$

For $\beta = \pi/2$, $u_C = 0$ according to equation 12. The measured Doppler shift is zero for particles moving perpendicular to the line-of-sight. To simplify the algebra, we take $m_\alpha = 4m_n$ and $m_C = 12m_n$. Using $1/\cos^2\beta - 1 = \tan^2\beta$ we find

$$\frac{Q^*}{6m_n} - v_\alpha^2 - 13\frac{u_C^2}{\cos^2\beta} + 8\Big(u_\alpha u_C + \cos\zeta\sqrt{(v_\alpha^2 - u_\alpha^2)u_C^2\tan^2\beta}\Big) = 0. \tag{17}$$

v_α and u_α are given by

$$v_\alpha^2 = v_\parallel^2 + v_\perp^2 \tag{18}$$

and [33]

$$u_\alpha = v_\parallel \cos\phi + v_\perp \sin\phi \cos\Gamma \tag{19}$$

where ϕ is the angle between the line-of-sight and the magnetic field at the position we consider as sketched in figure 4. Γ is the gyro-angle. Substitution gives

$$\frac{Q^*}{6m_n} - v_\parallel^2 - v_\perp^2 - 13\frac{u_C^2}{\cos^2\beta} + 8(v_\parallel \cos\phi + v_\perp \sin\phi\cos\Gamma)u_C$$
$$+8\cos\zeta\sqrt{(v_\parallel^2 + v_\perp^2 - (v_\parallel\cos\phi + v_\perp\sin\phi\cos\Gamma)^2)u_C^2\tan^2\beta} = 0. \tag{20}$$

This is an implicit functional relationship between the gyro-angle Γ of the alpha particle and the measurable u_C showing that the measurable energy E_γ depends on the gyro-angle Γ of the alpha particle for each point in 2D velocity space.

5. Analytic model of GRS probability functions

Equation 20 contains the gyroangle Γ which can take any value in $[0, 2\pi]$. The probability distribution is uniform to a good approximation:

$$\mathrm{pdf}_\Gamma = \frac{1}{2\pi}. \tag{21}$$

The relation between the measurable u_C and the gyroangle Γ of the alpha particle in equation 20 then allows us to calculate the probability that a detected γ-photon lies in a given energy range between $E_{\gamma,1}$ and $E_{\gamma,2}$ as we will show in this section. As this probability is a function of the observation angle ϕ and the position in velocity space, it is written as $\mathrm{prob}(E_{\gamma,1} < E_\gamma < E_{\gamma,2}|\phi, v_\parallel, v_\perp)$ where the conditioning symbol '|' means 'given'. The probability function is related to the weight function by a detection rate function $R(v_\parallel, v_\perp, \mathbf{x})$ defined as the detection rate of photons per alpha particle per second irrespective of the γ-ray energy in units [photons / (α-particle $\times$ s)]. The weight function w is obtained if we multiply the total detection rate per ion R with the probability that the detected γ-photon is in a particular energy range:

$$w(E_{\gamma,1}, E_{\gamma,2}, \phi, v_\parallel, v_\perp, \mathbf{x}) = R(v_\parallel, v_\perp, \mathbf{x}) \times \mathrm{prob}(E_{\gamma,1} < E_\gamma < E_{\gamma,2}|\phi, v_\parallel, v_\perp). \tag{22}$$

This relation has similarly been introduced to normalize FIDA and NES weight functions [32, 35]. $R(v_\parallel, v_\perp, \mathbf{x})$ hence has the same units as weight functions whereas the probabilities functions are dimensionless numbers between 0 and 1. $R(v_\parallel, v_\perp, \mathbf{x})$ depends on the production rate of γ-photons per alpha particle, on how many of the produced γ-photons reach the detector, and on how efficiently the γ-photons at the detector are detected. Energy and momentum conservation determine the boundaries of the probability functions $\mathrm{prob}(E_{\gamma,1} < E_\gamma < E_{\gamma,2}|\phi, v_\parallel, v_\perp)$ in $(v_\parallel, v_\perp)$-space and hence ultimately the boundaries of weight functions separating the observable regions from the unobservable regions. The amplitudes of the probability functions and the full weight functions also depend on the reaction cross sections.

We compute $R(v_\parallel, v_\perp, \mathbf{x})$ using the GENESIS code by allowing all possible E_γ:

$$R(v_{\parallel 0}, v_{\perp 0}, \mathbf{x}_0) = \frac{s_\delta(E_{\gamma,1} = 0, E_{\gamma,2} \to \infty, \phi)}{N_f}. \tag{23}$$

An example of a numerically calculated rate function for the $^9\mathrm{Be}(\alpha, \mathrm{n}\gamma)^{12}\mathrm{C}$ reaction is shown in figure 5. The rate function is, as the cross sections, symmetric in pitch angle. The numbers of detectable γ-photons per ion are enhanced at the resonances.

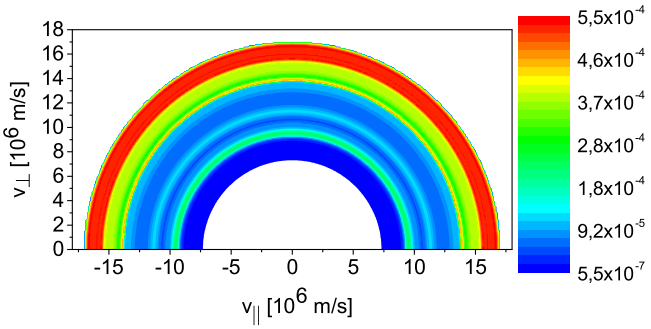

Figure 5. Rate function R [photons/(α-particle $\times$ s)] showing the number of detectable γ-photons per alpha particle at $\phi = 90°$ as a function of alpha particle velocities. The photons can have any energy. We assume $n_{Be} = 10^{18}$ m^{-3}. The resonances appear at $v = (9.5, 11.1, 13.8, 14.7, 15.5, 15.9, 16.6) \times 10^6$ m/s.

In the following we calculate probability functions introduced in equation 22 using equation 20. The angles β and ζ are random variables for which probability distribution functions $\mathrm{pdf}(\beta, \zeta | v_\parallel, v_\perp, \phi)$ can be computed numerically using the GENESIS code. The probability function $\mathrm{prob}(E_{\gamma,1} < E_\gamma < E_{\gamma,2} | v_\parallel, v_\perp, \phi)$ can be calculated by transforming to probabilities in u_C according to

$$\begin{aligned}
&\mathrm{prob}(E_{\gamma,1} < E_\gamma < E_{\gamma,2} | v_\parallel, v_\perp, \phi) \\
&= \mathrm{prob}(u_{C,1} < u_C < u_{C,2} | v_\parallel, v_\perp, \phi) \\
&= \int_{u_{C,1}}^{u_{C,2}} \mathrm{pdf}(u_C | v_\parallel, v_\perp, \phi) du_C \\
&= \int_{\beta,\zeta} \int_{u_{C,1}}^{u_{C,2}} \mathrm{pdf}(u_C | v_\parallel, v_\perp, \phi, \beta, \zeta) \mathrm{pdf}(\beta, \zeta | v_\parallel, v_\perp, \phi) du_C d\beta d\zeta
\end{aligned} \tag{24}$$

The integration limits in u_C can be directly calculated from equation 3 for the energy range of interest. The probability density function $\mathrm{pdf}(u_C | v_\parallel, v_\perp, \phi, \beta, \zeta)$ can be calculated by solving equation 20 for u_C and then by sampling from the uniform probability density function in gyro-angle Γ (equation 21).

To solve for u_C, we pull the always positive product $u_C \tan\beta$ in equation 17 in front of the square root:

$$\frac{Q^*}{6m_n} - v_\alpha^2 - 13\frac{u_C^2}{\cos^2\beta} + 8\left(u_\alpha u_C + u_C \tan\beta \sqrt{v_\alpha^2 - u_\alpha^2}\cos\zeta\right) = 0. \tag{25}$$

The solutions of the quadratic equation in u_C are

$$u_C = \frac{4}{13}\cos\beta\left(u_\alpha \cos\beta + \sin\beta\cos\zeta\sqrt{v_\alpha^2 - u_\alpha^2}\right)$$

$$\pm \sqrt{\frac{\cos^2\beta}{13}\left(\frac{16}{13}\left(u_\alpha\cos\beta+\sin\beta\cos\zeta\sqrt{v_\alpha^2-u_\alpha^2}\right)^2+\frac{Q^*}{6m_n}-v_\alpha^2\right)}. \quad (26)$$

A second option to calculate $\mathrm{prob}(E_{\gamma,1} < E_\gamma < E_{\gamma,2}|v_\parallel, v_\perp, \phi)$ is to transform the problem from u_C-space to Γ-space according to

$$\mathrm{pdf}(u_C|v_\parallel, v_\perp, \phi, \beta, \zeta) = \mathrm{pdf}_\Gamma\left|\frac{d\Gamma}{du_C}\right| \quad (27)$$

which has the advantage that the integration of the constant pdf_Γ is straightforward. Hence the probability function can alternatively be calculated according to

$$\begin{aligned}
&\mathrm{prob}(E_{\gamma,1} < E_\gamma < E_{\gamma,2}|v_\parallel, v_\perp, \phi)\\
&= \int_{\beta,\zeta}\sum_i\left|\int_{\Gamma_{1,i}}^{\Gamma_{2,i}}\mathrm{pdf}_\Gamma\mathrm{pdf}(\beta,\zeta|v_\parallel,v_\perp,\phi)d\Gamma\right|d\beta d\zeta\\
&= \int_{\beta,\zeta}\mathrm{pdf}(\beta,\zeta|v_\parallel,v_\perp,\phi)\sum_i\left|\int_{\Gamma_{1,i}}^{\Gamma_{2,i}}\mathrm{pdf}_\Gamma d\Gamma\right|d\beta d\zeta. \quad (28)
\end{aligned}$$

The integration limits in Γ must still be calculated. There are zero to four possible ranges in Γ corresponding to the range in u_C as we will show next. These are indicated as a sum over the index i in equation 28. As these ranges in Γ do not overlap, we sum over the mutually exclusive probabilities. We take the absolute value of the integral in Γ as the integral represents a probability and hence must be positive while we have $\Gamma_{1,i} > \Gamma_{2,i}$ for at least one interval, if there is a solution. In the last step we have used that $\mathrm{pdf}(\beta, \zeta|v_\parallel, v_\perp, \phi)$ does not depend on Γ. We can now evaluate the integral in Γ:

$$\begin{aligned}
&\mathrm{prob}(E_{\gamma,1} < E_\gamma < E_{\gamma,2}|v_\parallel, v_\perp, \phi)\\
&= \int_{\beta,\zeta}\mathrm{pdf}(\beta,\zeta|v_\parallel,v_\perp,\phi)\sum_i\left|\frac{\Gamma_{2,i}-\Gamma_{1,i}}{2\pi}\right|d\beta d\zeta \quad (29)
\end{aligned}$$

To find the integration limits in Γ in equations 28 and 29, we isolate the square root in equation 17 and square:

$$\begin{aligned}
&\left(\frac{Q^*}{6m_n}-v_\alpha^2-13\frac{u_C^2}{\cos^2\beta}\right)^2+16u_C\left(\frac{Q^*}{6m_n}-v_\alpha^2-13\frac{u_C^2}{\cos^2\beta}\right)u_\alpha+64u_C^2u_\alpha^2\\
&= 64u_C^2\tan^2\beta\cos^2\zeta\left(v_\alpha^2-u_\alpha^2\right). \quad (30)
\end{aligned}$$

The solutions in u_α are for $u_C\left(\cos^2\beta+\sin^2\beta\cos^2\zeta\right)\neq 0$

$$u_\alpha = \frac{13u_C^2+\cos^2\beta\left(v_\alpha^2-\frac{Q^*}{6m_n}\right)}{8u_C\left(\cos^2\beta+\sin^2\beta\cos^2\zeta\right)}$$

$$\pm\sqrt{\frac{\sin^2\beta\cos^2\zeta\left(64u_C^2v_\alpha^2\cos^2\beta\left(\cos^2\beta+\sin^2\beta\cos^2\zeta\right)-\left(\cos^2\beta\left(\frac{Q^*}{6m_n}-v_\alpha^2\right)-13u_C^2\right)^2\right)}{64u_C^2\cos^2\beta\left(\cos^2\beta+\sin^2\beta\cos^2\zeta\right)^2}}. \quad (31)$$

Γ is then found from u_α by

$$\Gamma = \arccos \frac{u_\alpha - v_\parallel \cos\phi}{v_\perp \sin\phi}. \tag{32}$$

A second pair of solutions for $\Gamma \in [\pi, 2\pi]$ is given by

$$\Gamma' = 2\pi - \Gamma \tag{33}$$

as $\cos(2\pi - \Gamma) = \cos\Gamma$ and the arccosine function is defined in $[0, \pi]$ whereas $\Gamma \in [0, 2\pi]$. This is the functional dependence between Γ and u_C required to transform the integration limits. However, taking the square again introduces a spurious solution, i.e. a solution of the squared equation 30 but not of the original non-squared equation 17, which we check for and exclude below.

We note that our solution for Γ is valid for not completely parallel observation ($\sin\phi \neq 0$), velocity-space positions not exactly on the $v_\parallel$-axis ($v_\perp \neq 0$), non-zero Doppler-shifts ($u_C \neq 0, \cos\beta \neq 0$), and particles not moving exactly parallel to the line-of-sight ($u_\alpha^2 \neq v_\alpha^2$ and $u_C^2 \neq v_C^2$). The special cases not fulfilling these conditions could be treated individually, but we omit these special cases for brevity.

6. Comparison of analytically and numerically calculated GRS probability functions for given (β, ζ)

In this section we compare probability functions for given (β, ζ) as computed by the analytical and the numerical approaches. Equation 28 shows that the full probability function $\mathrm{prob}(E_{\gamma,1} < E_\gamma < E_{\gamma,2}|v_\parallel, v_\perp, \phi)$ requires knowledge of the probability density function $\mathrm{pdf}(\beta, \zeta|v_\parallel, v_\perp, \phi)$. Nevertheless, equation 20 allows analytic computation of probability functions for given (β, ζ),

$$\mathrm{prob}(E_{\gamma,1} < E_\gamma < E_{\gamma,2}|\phi, v_\parallel, v_\perp, \beta, \zeta) = \sum_i \left| \frac{\Gamma_{2,i} - \Gamma_{1,i}}{2\pi} \right| \tag{34}$$

which must be integrated over (β, ζ) to obtain the full probability function:

$$\begin{aligned} &\mathrm{prob}(E_{\gamma,1} < E_\gamma < E_{\gamma,2}|v_\parallel, v_\perp, \phi) \\ &= \int_{\beta,\zeta} \mathrm{pdf}(\beta, \zeta|v_\parallel, v_\perp, \phi)\mathrm{prob}(E_{\gamma,1} < E_\gamma < E_{\gamma,2}|\phi, v_\parallel, v_\perp, \beta, \zeta) d\beta d\zeta \end{aligned} \tag{35}$$

Both probability functions can be calculated with the numerical approach. The full probability function can be calculated from the numerically calculated quantities w and R according to

$$\mathrm{prob}(E_{\gamma,1} < E_\gamma < E_{\gamma,2}|\phi, v_{\parallel 0}, v_{\perp 0}, \mathbf{x}_0) = \frac{w(E_{\gamma,1}, E_{\gamma,2}, \phi, v_{\parallel 0}, v_{\perp 0}, \mathbf{x}_0)}{R(v_{\parallel 0}, v_{\perp 0}, \mathbf{x}_0)}. \tag{36}$$

The probability $\mathrm{prob}(E_{\gamma,1} < E_\gamma < E_{\gamma,2}|\phi, v_\parallel, v_\perp, \beta, \zeta)$ can also be calculated using the numerical approach by allowing only the given (β, ζ)-pair:

$$\begin{aligned} \mathrm{prob}(E_{\gamma,1} < E_\gamma < E_{\gamma,2}|\phi, v_\parallel, v_\perp, \beta, \zeta) &= \frac{w(E_{\gamma,1}, E_{\gamma,2}, \phi, v_\parallel, v_\perp, \mathbf{x}, \beta, \zeta)}{R(v_\parallel, v_\perp, \mathbf{x}, \beta, \zeta)} \\ &= \frac{s(E_{\gamma,1}, E_{\gamma,2}, \phi, \beta, \zeta)}{N_f R(v_\parallel, v_\perp, \mathbf{x}, \beta, \zeta)}. \end{aligned} \tag{37}$$

As $\mathrm{pdf}(\beta, \zeta | v_\parallel, v_\perp, \phi)$ is not known analytically, it is best to compare analytic and the numerical approach at given (β, ζ). The probability functions $\mathrm{prob}(E_{\gamma,1} < E_\gamma < E_{\gamma,2} | \phi, v_\parallel, v_\perp, \beta, \zeta)$ may be regarded as basic building blocks of full probability functions $\mathrm{prob}(E_{\gamma,1} < E_\gamma < E_{\gamma,2} | \phi, v_\parallel, v_\perp)$. As probability functions based on equation 20 neglect the momentum and energy of the thermal beryllium impurity, we also neglect these in the numeric computation by setting the beryllium temperature to zero. A comparison of the analytical and numerical probability functions for given (β, ζ) is presented in figure 6. The amplitudes are the probabilities of detected γ-photons to be within the given energy range. The analytical and the numerical approaches find the complex shape of this probability function in very good agreement. The amplitudes of the analytical and numerical probability functions are slightly different because (β, ζ) are not given in exact values but rather in a small ranges due to the finite numerical resolution. We have calculated the probability functions up to energies of 6 MeV corresponding to 17×10^6 m/s as larger energies are usually not of interest. We have used this particular pair of (β, ζ) as this probability function has a particularly complex shape. The simpler shapes of probability functions for other (β, ζ) pairs computed with the numerical and the analytical approaches are similarly in very good agreement.

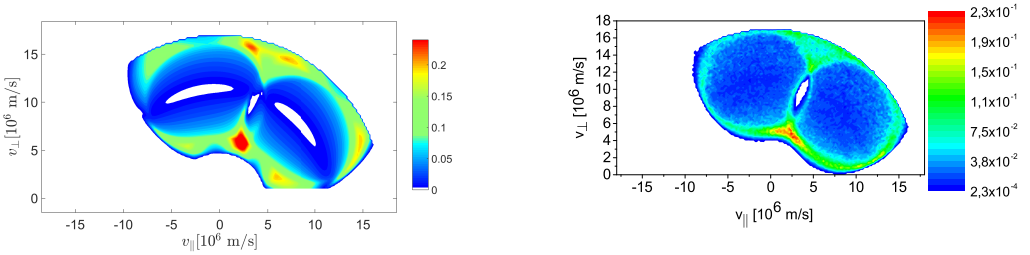

(a) Analytic (b) Numeric

Figure 6. $\mathrm{prob}(E_{\gamma,1} < E_\gamma < E_{\gamma,2} | \phi, v_\parallel, v_\perp, \beta, \zeta)$ for $E_\gamma = 15$ keV, $E_{\gamma 2} - E_{\gamma 1} = 1$ keV, $\phi = 30°$, $\beta = 70°$ and $\zeta = 10°$ as computed by the analytic and numerical approaches.

7. Parametric studies of the velocity-space sensitivity of GRS

In this section we study the velocity-space sensitivity of GRS measurements using simplified analytic expressions as shown in section 5. First we show examples of probability functions for fixed values of β and ζ. We will further present a simplified model for a full probability function by assuming a uniform probability distribution of (β, ζ).

Figure 7 shows the impact of the observation angle ϕ and the Doppler-shifted energy of the γ-rays for $\beta = \angle(\hat{\mathbf{v}}_{LOS}, \mathbf{v}_C) = 10°$ and $\zeta = \angle(\hat{\mathbf{v}}_{\perp\alpha,LOS}, \hat{\mathbf{v}}_{\perp C,LOS}) = 0°$. Typical observation angles for the two high-resolution GRS diagnostics at JET are $\phi = 90°$ and

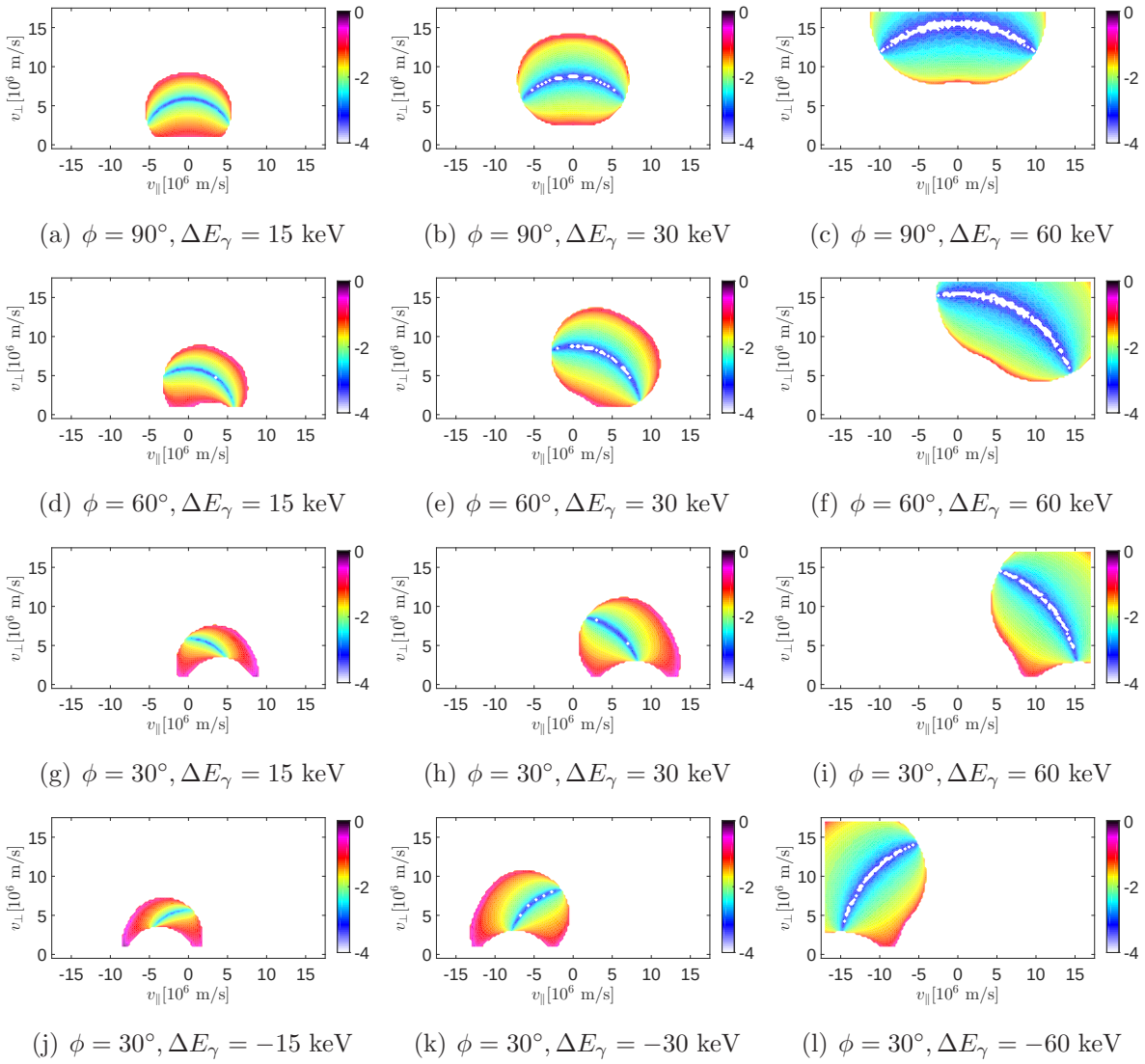

(a) $\phi = 90°, \Delta E_\gamma = 15$ keV (b) $\phi = 90°, \Delta E_\gamma = 30$ keV (c) $\phi = 90°, \Delta E_\gamma = 60$ keV

(d) $\phi = 60°, \Delta E_\gamma = 15$ keV (e) $\phi = 60°, \Delta E_\gamma = 30$ keV (f) $\phi = 60°, \Delta E_\gamma = 60$ keV

(g) $\phi = 30°, \Delta E_\gamma = 15$ keV (h) $\phi = 30°, \Delta E_\gamma = 30$ keV (i) $\phi = 30°, \Delta E_\gamma = 60$ keV

(j) $\phi = 30°, \Delta E_\gamma = -15$ keV (k) $\phi = 30°, \Delta E_\gamma = -30$ keV (l) $\phi = 30°, \Delta E_\gamma = -60$ keV

Figure 7. $\text{prob}(E_{\gamma,1} < E_\gamma < E_{\gamma,2}|\phi, v_\parallel, v_\perp, \beta, \zeta)$ for various projection angles $\phi = (30°, 60°, 90°)$ and Doppler shifts $\Delta E_\gamma = (-15, 15, 30, 60)$ keV in base ten logarithm, see subfigure captions. $E_{\gamma 2} - E_{\gamma 1} = 1.5$ keV and $\zeta = 0°$ are kept fixed. The angle between $\hat{\mathbf{v}}_{LOS}$ and $\mathbf{v}_C$ is set to $\beta = 10°$ for blueshift ($\Delta E_\gamma > 0$) and to the supplementary angle $\beta = 170°$ for redshift ($\Delta E_\gamma < 0$). The probability functions for redshift and blueshift with the same magnitude are mirror images about $v_\parallel = 0$.

$\phi = 30°$. The Doppler shifts of the γ-rays are varied from $\Delta E_\gamma = -15$ keV to $\Delta E_\gamma = 60$ keV corresponding to projected velocities of the ^{12}C from $u_C = -10^6$ m/s to $u_C = 4 \times 10^6$ m/s (equation 3). These values are also typical for GRS measurements at JET. Blueshifted γ-rays have positive ΔE_γ whereas redshifted γ-rays have negative ΔE_γ. The forms and positions of these probability functions $\text{prob}(E_{\gamma,1} < E_\gamma < E_{\gamma,2}|\phi, v_\parallel, v_\perp, \beta, \zeta)$ are highly dependent on the Doppler-shifted energies and the observation angles. The amplitudes of $\text{prob}(E_{\gamma,1} < E_\gamma < E_{\gamma,2}|\phi, v_\parallel, v_\perp, \beta, \zeta)$ are large near their boundaries. This is also observed for CTS, FIDA, and NES weight functions for the typical spectral resolution of the measurements and is explained by the projection of the circular gyro-

motion onto the line-of-sight which leads to high probabilities to observe velocities near the extremal values [32, 33, 35]. We further note the appearance of a low sensitivity region at a particular alpha particle energy in each probability function which does not occur for FIDA, CTS or NES weight functions. For $\phi = 90°$ (figures 7(a)-(c)) the probability functions are mirror symmetric about $v_\parallel = 0$ since $v_\parallel$ appears only as the squared quantity $v_\parallel^2$ in equation 20 whereas the linear terms in $v_\parallel$ vanish. The larger ΔE_γ is (or equivalently the larger u_C is), the larger the observable area covered by the probability functions is in alpha velocity space and the larger the velocities are. For the oblique line-of-sight with respect to the magnetic field at $\phi = 60°$ (figures 7(d)-(f)), a bias towards positive $v_\parallel$ for blueshifted E_γ is introduced into the probability functions. This bias comes from the terms $v_\parallel \cos\phi$ in equation 20. It becomes even stronger for $\phi = 30°$ (figures 7(g)-(i)). These biases for oblique lines-of-sight occur for any β and ζ and hence leave a signature in the full GRS weight functions and make GRS measurements with oblique lines-of-sight selective in pitch towards either co-going or counter-going alpha particles. Lastly, we find that the observation regions for given β and ζ and redshift are mirror images of those for corresponding blueshifts (figures 7(j)-(l)) as also follows from equation 20. Similarly, observation regions for fixed β and ζ for an observation angle $\phi' = 180° - \phi$ are mirror images to those at ϕ at the same Doppler shift.

In the following we calculate a simplified model of full probability functions $\mathrm{prob}(E_{\gamma,1} < E_\gamma < E_{\gamma,2}|\phi, v_\parallel, v_\perp)$ assuming that all angles β and ζ are equally likely. Then the $\mathrm{pdf}(\beta, \zeta|v_\parallel, v_\perp, \phi)$ is uniform. Our results show that salient features of the GRS weight functions in figure 2 are reflected in similar features of either the rate function R in figure 5 or the corresponding probability function. The elevated sensitivity of weight functions at the resonances is inherited from the rate functions. In contrast, the pitch selectivity is inherited from the probability functions $\mathrm{prob}(E_{\gamma,1} < E_\gamma < E_{\gamma,2}|\phi, v_\parallel, v_\perp)$.

In figure 8 we show a simplified model of the full probability function $\mathrm{prob}(E_{\gamma,1} < E_\gamma < E_{\gamma,2}|\phi, v_\parallel, v_\perp)$ for a perpendicular observation angle $\phi = 90°$ assuming uniform probability densities in (β, ζ). The Doppler shifts are varied from 15 keV to 75 keV. The boundaries of the simplified probability functions are identical with the boundaries of full probability functions computed with the GENESIS code whereas the amplitudes may be different for probability densities in (β, ζ) accounting for anisotropic cross sections. The probability functions reveal completely unobservable regions as well as local maxima with elevated sensitivity. The local maxima in the probability functions make the GRS measurements highly sensitive in particular pitch ranges whereas areas with no solution of energy and momentum equations make the GRS measurements completely insensitive in other pitch ranges. We note that the probability functions $\mathrm{prob}(E_{\gamma,1} < E_\gamma < E_{\gamma,2}|\phi, v_\parallel, v_\perp)$ presented here assume uniform probability densities in β and ζ in the allowed regions whereas in section 3 we fully accounted for the anisotropic differential cross sections.

For $\Delta E_\gamma = 15$ keV the entire velocity space is observable. The strong upper local maximum would suggest strong sensitivity for pitches near zero, but this maximum lies below the energy of the first resonance and is hence in a region producing few

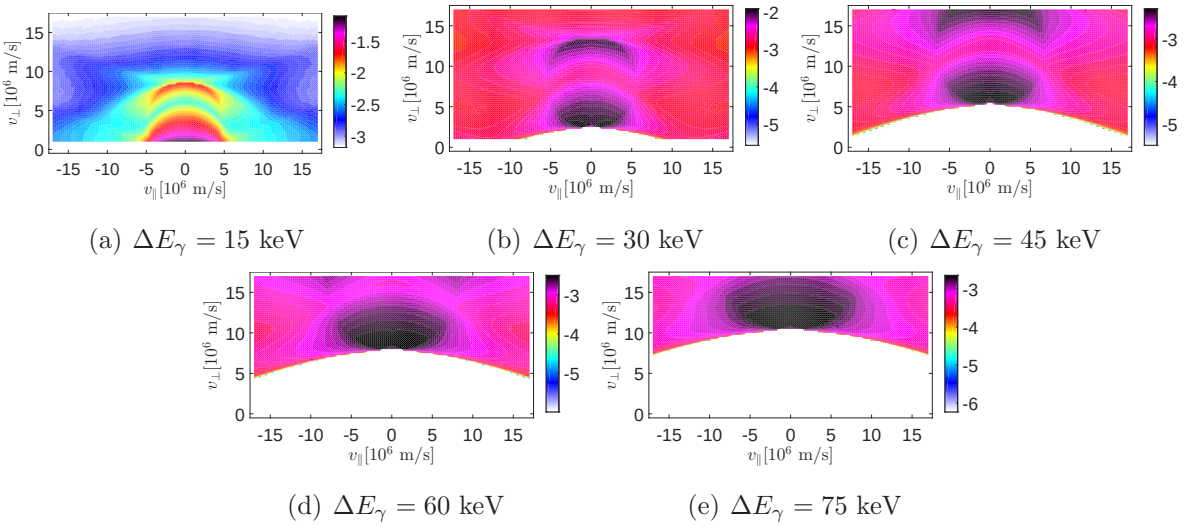

(a) $\Delta E_\gamma = 15$ keV (b) $\Delta E_\gamma = 30$ keV (c) $\Delta E_\gamma = 45$ keV

(d) $\Delta E_\gamma = 60$ keV (e) $\Delta E_\gamma = 75$ keV

Figure 8. prob$(E_{\gamma,1} < E_\gamma < E_{\gamma,2}|\phi, v_\parallel, v_\perp)$ assuming uniform probability densities in (β, ζ) for $\phi = 90°$ and various Doppler shifts $\Delta E_\gamma = (15, 30, 45, 60, 75)$ keV in base ten logarithm. $E_{\gamma 2} - E_{\gamma 1} = 1.5$ keV is kept fixed. Note that we choose different scales for each plot.

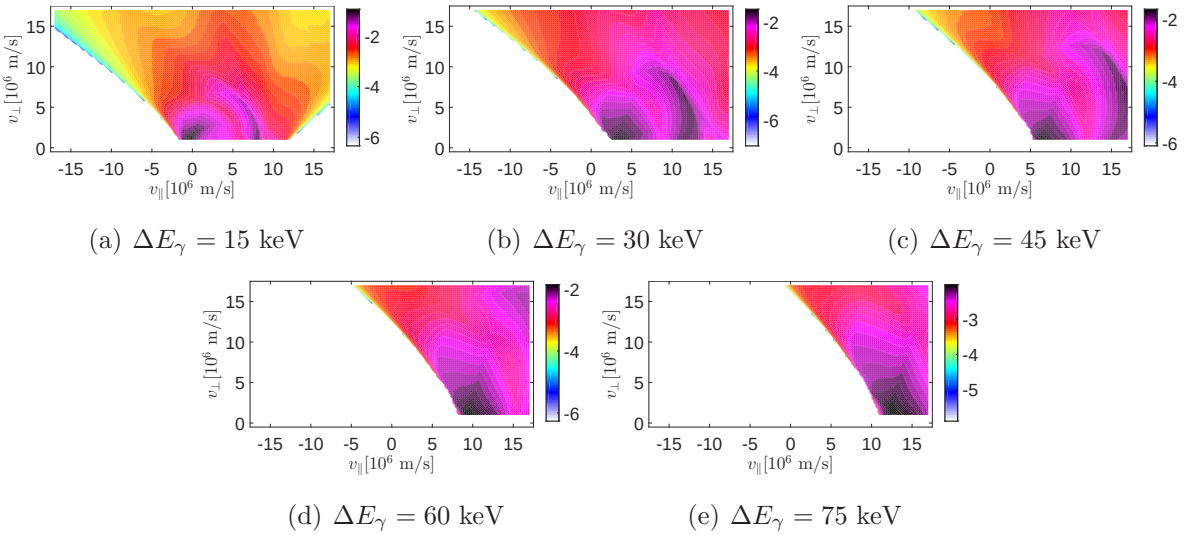

(a) $\Delta E_\gamma = 15$ keV (b) $\Delta E_\gamma = 30$ keV (c) $\Delta E_\gamma = 45$ keV

(d) $\Delta E_\gamma = 60$ keV (e) $\Delta E_\gamma = 75$ keV

Figure 9. prob$(E_{\gamma,1} < E_\gamma < E_{\gamma,2}|\phi, v_\parallel, v_\perp)$ assuming uniform probability densities in (β, ζ) for $\phi = 30°$ and various Doppler shifts $\Delta E_\gamma = (15, 30, 45, 60, 75)$ keV in base 10 logarithm. $E_{\gamma 2} - E_{\gamma 1} = 1.5$ keV is kept fixed. We assume uniform probability densities in (β, ζ). Note that choose different scales for each plot.

detectable γ-rays. For alpha particle energies larger than 1.9 MeV we find that the GRS measurements should be most sensitive to co-going and counter-going particles (low $v_\perp$) rather than trapped particles. This perhaps surprising result was also found by calculating full GRS weight functions in section 3. For larger Doppler shifts, completely unobservable regions appear at low $v_\perp$ (corresponding to pitches $\sim \pm 1$). In these regions energy and momentum conservation do not allow the emission of γ-photons with these

Doppler shifts. The sizes of these unobservable regions increase with the Doppler shift consistent with the corresponding weight functions. Further, there are particular regions with very large probabilities. We find two local maxima whose distances to the origin also increase with the Doppler shift. For $\Delta E_\gamma \sim 30$ keV the upper maximum lies in the region with significant γ-photon production whereas the lower maximum is still below the first resonance at 1.9 MeV. For $\Delta E_\gamma \sim 45$ keV the upper and lower local maxima at pitches around zero cover several resonances making the GRS measurements highly sensitive for pitches around zero. For $\Delta E_\gamma \sim 60$ keV the lower local maximum is in the region with significant γ-photon production. The elevated detection probabilities make GRS spectrometers observing at $\phi = 90°$ for Doppler shifts of about 45 keV or larger particularly sensitive to ions with pitches close to zero and rather insensitive or completely insensitive to ions with pitch close to ± 1. We stress that the most sensitive pitch range thus strongly depends on the Doppler shift.

We illustrate typical velocity-space observation regions of the other high-resolution γ-ray spectrometer at an observation angle $\phi = 30°$ and various Doppler shifts in figure 9. Completely unobservable regions appear even at small Doppler shifts ($\Delta E_\gamma \sim 15$ keV). These blueshifted γ-photons cannot be produced due to alpha particles with $p \sim -1$ and very high energy alpha particles with $p \sim 1$. Two local maxima with elevated detection probabilities again appear that are biased towards positive $v_\parallel$ for blueshift and $\phi = 30°$. Further we find elevated probabilities for pitches near zero explaining why the weight functions for low Doppler shift and $\phi = 30°$ are actually most sensitive to trapped particles. For Doppler shifts of $\Delta E_\gamma \gtrsim 30$ keV, the probability functions show the expected bias. The blueshifted side is most sensitive to co-going particles. For large Doppler shifts the measurement is not sensitive to counter-going particles at all. The probabilities are also rather small for trapped alpha particles. As already mentioned GRS weight functions for redshifts are mirror images of those with the corresponding blueshift.

8. Applications of GRS weight functions for a slowing-down distribution

Traditionally high resolution GRS spectra are calculated by computationally demanding Monte Carlo simulation using the GENESIS code. GRS spectra can also be calculated using weight functions. In this approach weight functions are calculated for each Doppler-shifted energy bin. Once the weight functions are known, the spectra can be rapidly calculated by matrix multiplication for any f. The matrix multiplication method is significantly faster than the Monte Carlo simulation [32,33,35]. This becomes very advantageous if spectra for many distributions functions are to be calculated. We illustrate the two approaches to calculate spectra for an alpha particle slowing down distribution. This distribution is illustrated in figure 10 as a slice of a 3D function $[s^3/m^6]$ and as 2D function with no implied third direction $[s^2/m^5]$. The slowing down

distribution is given by

$$f^{3D}(v_\parallel, v_\perp) = \frac{\tau_s}{(v_\parallel^2 + v_\perp^2)^{3/2} + v_c^3} \int_0^\infty \tilde{v}^2 S(\tilde{v}) d\tilde{v} \tag{38}$$

where τ_s is the slowing-down time, v_c is the critical velocity and S is the alpha particle source spectrum, which we calculated using a Monte Carlo approach.

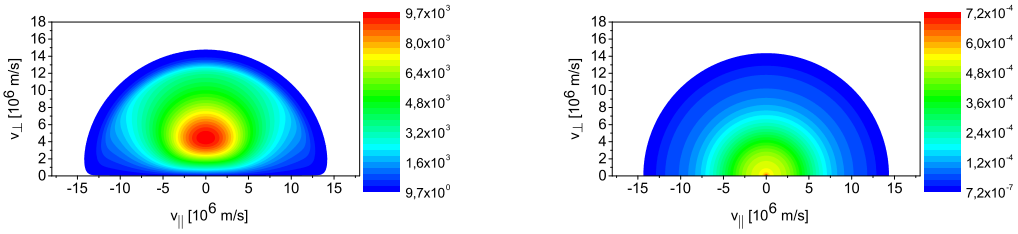

Figure 10. Alpha particle slowing-down distribution represented (left) as a slice of a 3D function $[s^3/m^6]$ and (right) as 2D function $[s^2/m^5]$. We assume $n_\alpha = 10^{18}$ m^{-3}, $n_e = 10^{20}$ m^{-3}, $n_D = n_T = n_e/2$ and $T_D = T_T = T_e = 20$ keV. The velocity distribution function f^{2D} from f^{3D} by transforming to cylindrical coordinates and integrating over the by assumption ignorable gyroangle Γ, $f^{2D} = 2\pi v_\perp f^{3D}$.

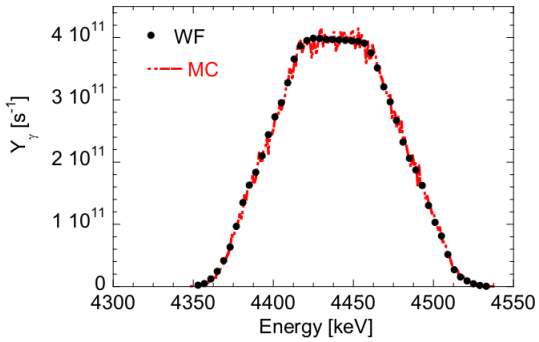

Figure 11. Energy spectrum for the $E_{\gamma 0} = 4.44$ MeV level for the alpha particle slowing-down distribution from figure 10 as calculated using Monte Carlo simulations (MC) and by weight functions (WF). The spectrum shows the number of detected γ-photons per second [photons /s] in small energy bins of widths $E_{\gamma,2} - E_{\gamma,1} = 1$ keV. We assume emission from a point source in position space.

Figure 11 demonstrates that spectra calculated using weight functions and using the Monte Carlo approach agree within the Monte Carlo noise level. This verifies that the GRS weight functions are in agreement with the traditional Monte Carlo simulation. The weight function method additionally shows the alpha particle velocity space origin of the signal in a particular γ-photon energy bin. This is shown by the product of the particular weight function for this γ-photon energy bin and the fast-ion velocity distribution function $w \times f$ at that point. Figures 12 and 13 illustrate these regions for $\phi = 90°$ and $\phi = 30°$ for a few Doppler-shifted energies, respectively. For the adopted slowing-down distribution, most γ-photons with Doppler shifts below $\lesssim 60$ keV are

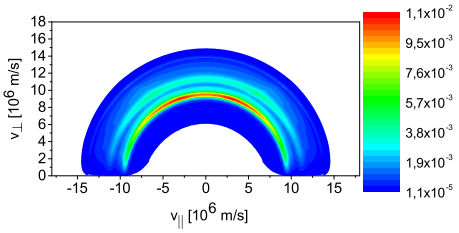

(a) $\Delta E_\gamma = -15$ keV

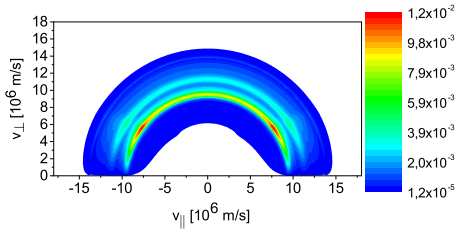

(b) $\Delta E_\gamma = 0$ keV

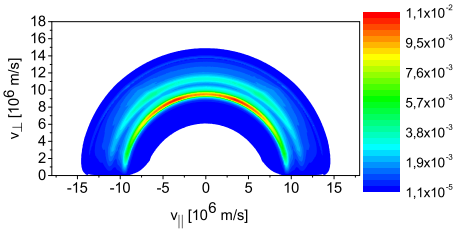

(c) $\Delta E_\gamma = 15$ keV

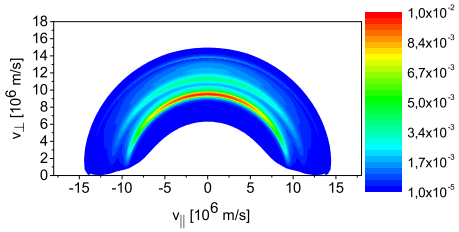

(d) $\Delta E_\gamma = 30$ keV

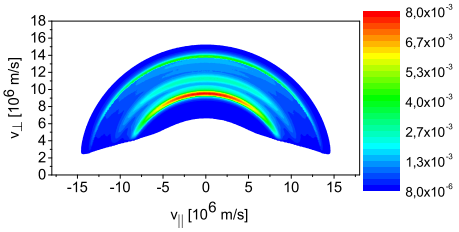

(e) $\Delta E_\gamma = 45$ keV

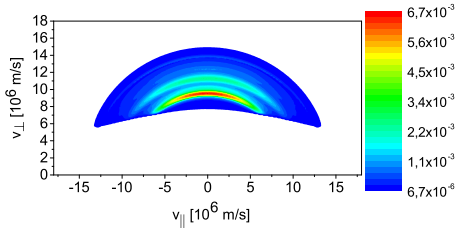

(f) $\Delta E_\gamma = 60$ keV

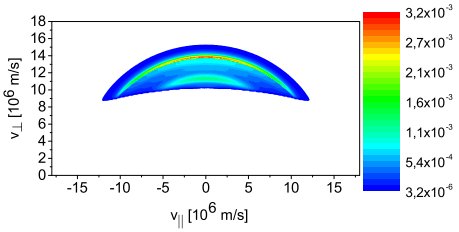

(g) $\Delta E_\gamma = 75$ keV

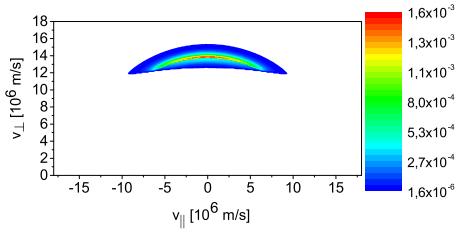

(h) $\Delta E_\gamma = 90$ keV

Figure 12. The products $w \times f$ of the functions shown in figures 2 and 10b illustrate how many γ-photons detected at each Doppler shift ΔE_γ were produced resolved in 2D velocity-space for this slowing-down distribution function. The units are [photons $\times$ s / m^5]. The γ-ray energy bin width is $E_{\gamma,1} - E_{\gamma,2} = 1$ keV, and the observation angle is $\phi = 90°$. We assume $n_{Be} = 10^{18}$ m^{-3} and $T_{Be} = 0$ keV.

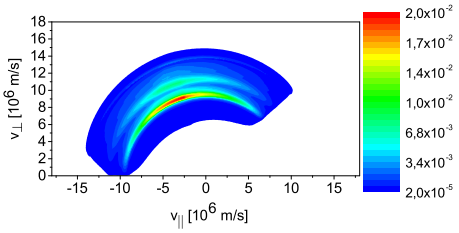

(a) $\Delta E_\gamma = -15$ keV

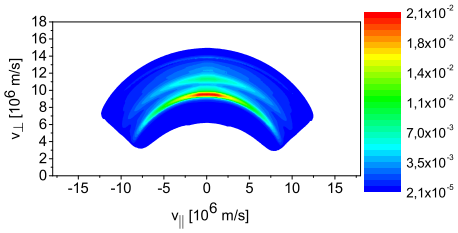

(b) $\Delta E_\gamma = 0$ keV

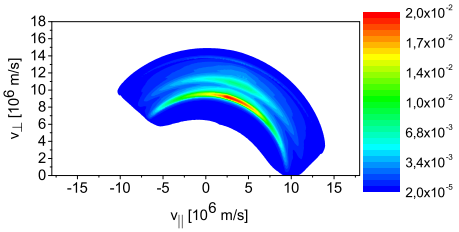

(c) $\Delta E_\gamma = 15$ keV

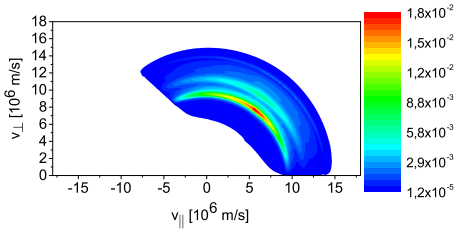

(d) $\Delta E_\gamma = 30$ keV

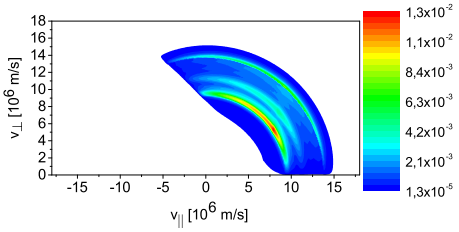

(e) $\Delta E_\gamma = 45$ keV

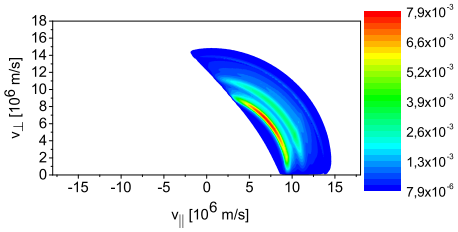

(f) $\Delta E_\gamma = 60$ keV

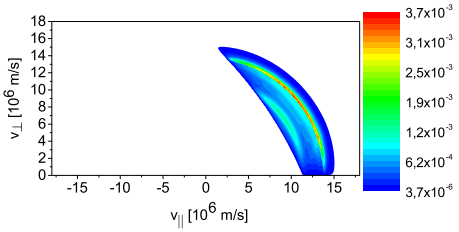

(g) $\Delta E_\gamma = 75$ keV

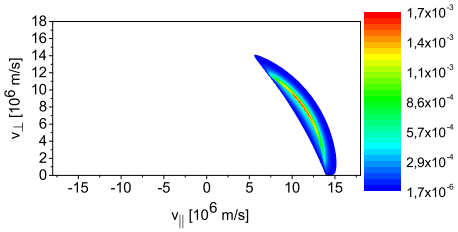

(h) $\Delta E_\gamma = 90$ keV

Figure 13. The products $w \times f$ of the functions shown in figures 3 and 10b illustrate how many γ-photons detected at each Doppler shift ΔE_γ were produced resolved in 2D velocity-space for this slowing-down distribution function. The units are [photons $\times$ s / m^5]. The γ-ray energy bin width is $E_{\gamma,1} - E_{\gamma,2} = 1$ keV, and the observation angle is $\phi = 30°$. We assume $n_{Be} = 10^{18}$ m^{-3} and $T_{Be} = 0$ keV.

produced near the 1.9 MeV resonance. Most γ-photons with Doppler shifts larger than 60 keV are produced near the 4 MeV resonance as energy and momentum conservation do not permit the production of γ at the 1.9 MeV resonance. We further find the strong pitch dependence inherited from the corresponding weight functions.

9. Discussion

Weight functions are widely used to interpret FIDA and CTS measurements [31–35, 41–61]. Recently, NES weight functions have been derived and applied to interpret measurements with the time-of-flight neutron spectrometer TOFOR at JET [34, 35]. GRS weight functions should likewise prove useful for GRS measurements at JET. Alpha particles accelerated to high energies by ICRH likely have pitches quite close to zero and can hence be measured well using the detector with the perpendicular line-of-sight ($\phi = 90°$) at large Doppler shifts. However, alpha particles generated in burning plasma in the upcoming DT campaign at JET should be quite evenly distributed in pitch. GRS weight functions show that measurements at $\phi = 90°$ and large Doppler shifts will preferentially detect trapped fast particles with low pitches ($p \sim 0$) whereas measurements at $\phi = 30°$ and large Doppler shifts will preferentially detect co- and counter-going fast particles on the blue- and redshifted sides of the peak, respectively.

Weight functions are further used to measure 2D fast-ion distribution functions by tomographic inversion. This was demonstrated for FIDA measurements at ASDEX Upgrade in NBI heated MHD quiescent discharges as well as discharges with sawtooth activity. JET has two high-resolution γ-ray spectrometers as well as two high-resolution neutron emission spectrometers. These diagnostics could be combined to measure 2D fast-ion distribution functions in JET discharges. This could provide direct measurements of 2D velocity distribution functions of fast ions in the MeV range generated by ICRH or even of an alpha distribution function in burning plasma in the upcoming DT campaign at JET. However, this is beyond the scope of this paper. We must still investigate if the signal-to-noise ratio is high enough for tomographic inversion. Further, GRS and NES measurements have no spatial resolution along their lines-of-sight, and hence measurements in small spatial volumes as for FIDA are not possible with this diagnostic set. At JET the tomographic inversion would determine a spatial average of the 2D velocity distribution function in the plasma core assuming most fusion products are formed there.

GRS weight functions could also prove useful for tomographic inversion at ASDEX Upgrade [67, 68] where up to six FIDA views [39, 55, 61], two CTS views [54, 62, 69–73], one NES view [74, 75], one GRS view [22], one neutral particle analyzer as well as three FILD diagnostics [76, 77] provide excellent fast-ion velocity-space coverage. Here the GRS weight functions enable us to use GRS together with the other diagnostics to measure 2D fast-ion distribution functions.

Lastly, our formalism will show the velocity-space sensitivity of GRS measurements on ITER [24] and DEMO [25] and fusion reactors beyond. ITER will also be equipped

with NES [78] and CTS [79–81] diagnostics, and diagnostics based on charge-exchange reactions will also likely give valuable information about fast ions [82]. GRS weight functions should make it possible to measure 2D fast-ion velocity distribution functions on ITER in combination with the other fast-ion diagnostics.

10. Conclusions

Here we calculated weight functions revealing velocity-space sensitivities of GRS measurements. GRS weight functions show how many γ-photons can be detected per ion and hence which velocity-space regions are observable and which are unobservable. Given a simulated fast-ion distribution function, GRS weight functions allow rapid calculation of γ-ray spectra additionally showing how many γ-rays are produced for each alpha particle velocity. We focussed on the ^{9}Be(α,nγ)^{12}C reaction, but our formalism is valid for any two-step reaction producing γ-rays.

It is known that GRS measurements of the ^{9}Be(α,nγ)^{12}C reaction are highly sensitive to alpha particles with energies near the resonance energies of the reaction. Here we demonstrate that the GRS measurements are also highly selective in pitch depending on the orientation of the line-of-sight and the Doppler-shifted energy. The pitch selectivity originates from the conservation of energy and momentum and the Doppler shift condition as we demonstrate by constructing a tractable simplified model.

The two high-resolution γ-ray spectrometers at JET have a perpendicular ($\phi = 90°$) and an oblique line-of-sight ($\phi = 30°$) with respect to the central magnetic field, respectively. GRS measurements with perpendicular lines-of-sight are highly sensitive to ions with pitches close to zero for large Doppler shifts. Perhaps surprisingly, for small Doppler shifts they are most sensitive to ions with pitch close to ± 1. On the contrary, for the oblique lines-of-sight the blueshifted side of the spectrum is sensitive to co-going ions and the redshifted to counter-going ions for large Doppler shifts. At very large Doppler shifts, these measurements are completely insensitive not only to ions passing in the opposite direction but even to ions with pitches near zero. For smaller Doppler shifts the measurements are biased in the same sense but still sensitive to both sides of the spectrum. Again perhaps surprisingly, measurements for the oblique line-of-sight at small Doppler shifts are most sensitive to particles with pitches around zero.

The energy selectivity and pitch selectivity make GRS measurements highly sensitive in rather small regions in velocity space. This selectivity in 2D velocity space suggests that GRS measurements could be highly valuable in measurements of 2D velocity distribution functions by tomographic inversion.

Acknowledgments

This work has been carried out within the framework of the EUROfusion Consortium and has received funding from the Euratom research and training programme 2014-2018 under grant agreement No 633053. The views and opinions expressed herein do

not necessarily reflect those of the European Commission.

References

[1] Kiptily V G, Cecil F E and Medley S S 2006 *Plasma Phys. Control. Fusion* **48** R59–R82
[2] Tardocchi M, Nocente M and Gorini G 2013 *Plasma Phys. Control. Fusion* **55** 074014
[3] Newman D E and Cecil F 1984 *Nucl. Instrum. Meth. Phys. Res. A* **227** 339–341
[4] Cecil F E and Medley S S 1988 *Nucl. Instrum. Meth. Phys. Res. A* **271** 628–635
[5] Boyd D A *et al* 1989 *Nucl. Fusion* **29** 593–604
[6] Jarvis O N *et al* 1996 *Nucl. Fusion* **36** 1513–1530
[7] Kiptily V G, Cecil F E, Jarvis O N and Mantsinen M J 2002 *Nucl. Fusion* **42** 999–1007
[8] Kiptily V G *et al* 2003 *Rev. Sci. Instrum.* **74** 1753
[9] Kiptily V G *et al* 2004 *Physical Review Letters* **93** 115001
[10] Kiptily V G *et al* 2005 *Nucl. Fusion* **45** L21–L25
[11] Kiptily V G *et al* 2009 *Nucl. Fusion* **49** 065030
[12] Kiptily V G *et al* 2012 *Plasma Phys. Control. Fusion* **54** 074010
[13] Kiptily V G *et al* 2013 *Plasma and Fusion Research* **8** 2502071
[14] Kondoh T *et al* 1997 *Journal of Nuclear Materials* **241-243** 564–568
[15] Nishitani T, Tobita K, Kusama Y and Shibata Y 2001 *Rev. Sci. Instrum.* **72** 877
[16] Kiptily V G *et al* 2010 *Nucl. Fusion* **50** 084001
[17] Murari A *et al* 2010 *Rev. Sci. Instrum.* **81** 10E136
[18] Nocente M *et al* 2010 *Rev. Sci. Instrum.* **81** 10D321
[19] Nocente M *et al* 2012 *Nucl. Fusion* **52** 063009
[20] Tardocchi M *et al* 2011 *Physical Review Letters* **107** 205002
[21] Shevelev A E *et al* 2013 *Nucl. Fusion* **53** 123004
[22] Nocente M *et al* 2012 *Nucl. Fusion* **52** 094021
[23] Nocente M *et al* 2013 *IEEE Transactions on Nuclear Science* **60** 1408–1415
[24] Chugunov I N *et al* 2011 *Nucl. Fusion* **51** 083010
[25] Kiptily V 2015 *Nucl. Fusion* **55** 023008
[26] Cecil F, Zweben S and Medley S 1986 *Nucl. Instrum. Meth. Phys. Res. A* **245** 547–552
[27] Kiptilyj V G 1990 *Fusion Science and Technology* **18** 583–590
[28] Romanelli F 2013 *Nucl. Fusion* **53** 104002
[29] Romanelli F 2015 *Nucl. Fusion* **55** 104001
[30] Ajzenberg-Selove F 1991 *Nuclear Physics A* **523** 1–196 ISSN 03759474
[31] Heidbrink W W *et al* 2007 *Plasma Phys. Control. Fusion* **49** 1457–1475
[32] Salewski M *et al* 2014 *Plasma Phys. Control. Fusion* **56** 105005
[33] Salewski M *et al* 2011 *Nucl. Fusion* **51** 083014
[34] Jacobsen A S *et al* 2014 *Rev. Sci. Instrum.* **85** 11E103
[35] Jacobsen A S *et al* 2015 *Nucl. Fusion* **55** 053013
[36] Salewski M *et al* 2012 *Nucl. Fusion* **52** 103008
[37] Salewski M *et al* 2015 *Plasma Phys. Control. Fusion* **57** 014021
[38] Salewski M *et al* 2014 *Nucl. Fusion* **54** 023005
[39] Geiger B *et al* 2015 *Nucl. Fusion* **55** 083001
[40] Salewski M *et al* 2013 *Nucl. Fusion* **53** 063019
[41] Heidbrink W W 2010 *Rev. Sci. Instrum.* **81** 10D727
[42] Geiger B *et al* 2014 *Nucl. Fusion* **54** 022005
[43] B Geiger 2013 *Fast-ion transport studies using FIDA spectroscopy at the ASDEX Upgrade tokamak* Phd Ludwig-Maximilians-Universität München
[44] Heidbrink W W *et al* 2006 *Rev. Sci. Instrum.* **77** 10F120
[45] Luo Y *et al* 2007 *Rev. Sci. Instrum.* **78** 033505
[46] Podestà M *et al* 2008 *Rev. Sci. Instrum.* **79** 10E521

[47] Van Zeeland M A *et al* 2009 *Plasma Phys. Control. Fusion* **51** 055001
[48] Van Zeeland M A *et al* 2010 *Nucl. Fusion* **50** 084002
[49] Bortolon A *et al* 2010 *Rev. Sci. Instrum.* **81** 10D728 ISSN 1089-7623
[50] Heidbrink W W *et al* 2011 *Plasma Phys. Control. Fusion* **53** 085007
[51] Michael C A *et al* 2013 *Plasma Phys. Control. Fusion* **55** 095007
[52] Jones O M *et al* 2014 *arXiv:1401.6864*
[53] Heidbrink W W *et al* 2014 *Plasma Phys. Control. Fusion* **56** 095030
[54] Nielsen S K *et al* 2015 *Plasma Phys. Control. Fusion* **57** 035009
[55] Geiger B *et al* 2015 *Plasma Phys. Control. Fusion* **57** 014018
[56] Heidbrink W W *et al* 2008 *Rev. Sci. Instrum.* **79** 10E520
[57] Podesta M *et al* 2009 *Physics of Plasmas* **16** 056104
[58] Garcia-Munoz M *et al* 2011 *Nucl. Fusion* **51** 103013
[59] Geiger B *et al* 2011 *Plasma Phys. Control. Fusion* **53** 065010
[60] Muscatello C M *et al* 2012 *Plasma Phys. Control. Fusion* **54** 025006
[61] Geiger B *et al* 2013 *Rev. Sci. Instrum.* **84** 113502
[62] Rasmussen J *et al* 2015 *Plasma Phys. Control. Fusion* **57** 075014
[63] Pace D C *et al* 2013 *Physics of Plasmas* **20** 056108
[64] Nocente M 2012 *Neutron and gamma-ray emission spectroscopy as fast ion diagnostics in fusion plasmas* Ph.D. thesis URL `https://boa.unimib.it/handle/10281/28397`
[65] Proverbio I *et al* 2010 *Rev. Sci. Instrum.* **81** 10D320
[66] Kozlovsky B *et al* 2002 *The Astrophysical Journal Supplement Series* **141** 523–541
[67] Stroth U *et al* 2013 *Nucl. Fusion* **53** 104003
[68] Zohm H 2015 *Nucl. Fusion* **55** 104010
[69] Meo F *et al* 2008 *Rev. Sci. Instrum.* **79** 10E501
[70] Meo F *et al* 2010 *J. Phys.: Conf. Ser.* **227** 012010
[71] Salewski M *et al* 2010 *Nucl. Fusion* **50** 035012
[72] Furtula V *et al* 2012 *Rev. Sci. Instrum.* **83** 013507
[73] Stejner M *et al* 2015 *Plasma Phys. Control. Fusion* **57** 062001
[74] Tardini G *et al* 2012 *Journal of Instrumentation* **7** C03004–C03004
[75] Tardini G *et al* 2013 *Nucl. Fusion* **53** 063027
[76] Garcia-Munoz M *et al* 2013 *Nucl. Fusion* **53** 123008
[77] Garcia-Munoz M *et al* 2013 *Plasma Phys. Control. Fusion* **55** 124014
[78] Donné A J H *et al* Progress in the ITER Physics Basis Chapter 7: Diagnostics 2007 *Nucl. Fusion* **47** S337–S384
[79] Salewski M *et al* 2008 *Rev. Sci. Instrum.* **79** 10E729
[80] Salewski M *et al* 2009 *Plasma Phys. Control. Fusion* **51** 035006
[81] Salewski M *et al* 2009 *Nucl. Fusion* **49** 025006
[82] Kappatou A *et al* 2012 *Nucl. Fusion* **52** 043007